Cement & Concrete Composites 30 (2008) 686–699

Contents lists available at ScienceDirect

Cement & Concrete Composites

journal homepage: www.elsevier.com/locate/cemconcomp

# Microstructure engineering of Portland cement pastes and mortars through addition of ultrafine layer silicates

Holger Lindgreen [a,*], Mette Geiker [b], Hanne Krøyer [c], Niels Springer [d], Jørgen Skibsted [c]

[a] Clay Mineralogical Laboratory, Geological Survey of Denmark and Greenland, Øster Voldgade 10, DK-1350 Copenhagen K, Denmark
[b] Department of Civil Engineering (DTU) and Nano DTU, Technical University of Denmark, Brovej, Building 118, DK-2800 Kgs. Lyngby, Denmark
[c] Instrument Centre for Solid-State NMR Spectroscopy and Interdisciplinary Nanoscience Center (iNANO), Department of Chemistry, University of Aarhus, DK-8000 Aarhus C, Denmark
[d] Core Laboratory, Geological Survey of Denmark and Greenland, Øster Voldgade 10, DK-1350 Copenhagen K, Denmark

ARTICLE INFO

*Article history:*
Received 29 May 2006
Received in revised form 14 March 2008
Accepted 8 May 2008
Available online 21 May 2008

*Keywords:*
Cement
Paste
Mortar
Clay
Layer silicate
Silica fume
Additives
Nano
Structure engineering
Porosity
Atomic force microscopy

ABSTRACT

Pozzolanic submicron-sized silica fume and the non-pozzolanic micron- and nano-sized layer silicates (clay minerals) kaolinite, smectite and palygorskite have been used as additives in Portland cement pastes and mortars. These layer silicates have different particle shape (needles and plates), surface charge, and size (micron and nano). The structure of the resulting cement pastes and mortars has been investigated by atomic force microscopy (AFM), helium porosimetry, nitrogen adsorption (specific surface area and porosity), low-temperature calorimetry (LTC) and thermal analysis. The main result is that the cement paste structure and porosity can be engineered by addition of selected layer silicates having specific particle shapes and surface properties (e.g., charge and specific surface area). This seems to be due to the growth of calcium-silicate-hydrates (C–S–H) on the clay particle surfaces, and the nano-structure of the C–S–H depends on type of layer silicate. The effect of layer silicate addition is most pronounced for palygorskite and smectite having the largest surface area and negative charges on the particle surfaces. The cement pastes containing palygorskite and bentonite have, in comparison to the pure cement paste and the paste containing kaolinite, a more open pore structure consisting of fine pores. Silica fume paste contains a significant amount of closed pores. As a secondary result, it is demonstrated that both the degree and duration of sample drying strongly modifies the structure of the cementitious materials under investigation.



## 1. Introduction

Engineering the pore structure is important for designing concrete with specific properties. The pore structure of concrete strongly influences both mechanical behaviour and transport properties, which are essential for the durability of the concrete [1]. Addition of micro- and nano-particles to cementitious mixtures may result in a more homogeneous and finer pore structure. This is due to an improved initial packing of the solids and nucleation of hydration products on the surfaces of the fine particles (filler effect). In addition, some siliceous (or siliceous and aluminous) fine particles, such as silica fume ($SiO_2$) and metakaolin ($Al_2Si_2O_7$), react with calcium hydroxide and form hydration products with cementitious properties (pozzolanic effect).

In concretes based on Portland cement, water and aggregate, products of cement hydration gradually fill some of the interparticle space. The main hydration product, the calcium silicate hydrate (C–S–H) phase, is a composite of a nano-sized solid-phase and nano-sized pores, see e.g. [2,3], and it is often assumed that the large surface area of cementitious materials can be attributed to the properties of the C–S–H phase [3].

The C–S–H is a poorly crystalline phase which has a layer structure that ideally resembles the atomic structures for the crystalline 11 Å and 14 Å tobermorites [2,4,5]. The microstructure of the C–S–H has been described by different models. According to an early model [4] and in agreement with the Feldman–Sereda model [6], the microstructure of the C–S–H is related to the layered structures of tobermorite and jennite. Consequently, interlayer spacings containing strongly adsorbed water were assumed to be present in the C–S–H. The Feldman–Sereda model [6] is such a model. An alternative, colloidal-based model for two types of C–S–H has more recently been proposed by Jennings [7] and Tennis and Jennings [8]. The two types of C–S–H are a low-density (LD) C–S–H consisting of flocculated globules and a high-density (HD) C–S–H with closely packed globules. This model assumes that the LD C–S–H is the only component in Portland cement pastes that contributes significantly to the specific surface area measured by nitrogen adsorption, whereas in the HD C–S–H few pores are accessible to nitrogen at 77 K [9]. However, the LD C–S–H contains a significant

* Corresponding author. Tel.: +45 38142913; fax: +45 39142050.
*E-mail address:* hl@geus.dk (H. Lindgreen).

0958-9465/$ - see front matter © 2008 Elsevier Ltd. All rights reserved.
doi:10.1016/j.cemconcomp.2008.05.003

proportion of porosity which is normally not accessible to nitrogen at 77 K, most likely due to slow diffusion (activated entry). Water molecules can probably enter both LD and HD C–S–H [9]. During cement hydration, an inner hydration shell and an outer hydration shell are formed within the original cement grains. Besides, C–S–H nucleates in the solution. Scrivener [10] correlated the LD and HD C–S–H of Tennis and Jennings [8] to the outer and inner hydration products, respectively, as observed in backscattered electron images, and attributed the C–S–H formed in solution to the LD C–S–H.

Addition of pozzolans, e.g. silica fume, to Portland cement increases the quantity of the C–S–H phase on the account of the amount of calcium hydroxide. Addition of silica fume reduces the capillary porosity and densifies the microstructure of the interfacial transition zone (ITZ) between the bulk cement paste and aggregates [11]. Furthermore, the pozzolanic reaction appears to produce a C–S–H with a significantly lower diffusivity compared to C–S–H phases formed in cement pastes without silica fume addition [11]. A possible negative consequence of the dense microstructure observed in concretes based on addition of silica fume and a low water/cement ratio (w/c) is that these concretes may show explosive spalling during high-temperature loading [12–14].

The sub-micron sized particles used in concrete production have so far predominantly been silica fume. Micro- or nano-sized layer silicates exhibit no pozzolanic reactions in Portland cement systems [15]. However, addition of these silicates to Portland cements accelerates the cement hydration [15–17] by increasing the degrees of hydration for both alite and belite [17]. Moreover, it has been shown that replacement of 20 wt.% of the Portland cement by a kaolinite or illitic clay results in an increased porosity of paste samples, but a decreased porosity of mortars as measured by mercury intrusion porosimetry [18]. A decrease in compressive strength of mortars following addition of illite, smectite, kaolinite or illite–smectite was observed by He et al. [19,20]. The partly contradictive data from the above mentioned investigations may to some extent reflect varying degrees of dispersion of the clay materials in the cement mixtures. In a solid-state $^{29}Si$ MAS NMR investigation [15], it was found that two layer silicates, smectite and kaolinite, result in formation of different nano-structures of the silicates formed during the hydration, i.e. shorter and longer average chain lengths of $SiO_4$-tetrahedra for the C–S–H in mixtures containing smectite and kaolinite, respectively.

To design new types of concrete, we have applied non-pozzolanic micro- and nano-size layer silicates (kaolinite, smectite and palygorskite) as additives in concrete. Previously, we have described the molecular structure of the C–S–H hydration products for these new materials [15]. The aim of the present investigation is an evaluation of the influence of the selected types of micro- and nano-sized additives on porosity characteristics of pastes and mortars, including the effect on the ITZ between aggregate and bulk cement paste. The paper describes experimental investigations of the structure and pore systems obtained using these new additive materials compared to the pore systems of pastes and mortars with pure cement and with cement added silica fume. The micro-/nano-structures have been investigated by atomic force microscopy (AFM) on freshly fractured paste samples. Determination of helium-porosity and nitrogen adsorption specific surface area and porosity have been applied to determine the amount of open pores in pastes and mortars and these results are compared to the total amount of pores estimated from density measurements.

Furthermore, low-temperature calorimetry (LTC) has been carried out for mortars to determine the porosity characteristics. For the cement paste samples, non-evaporable, physically adsorbed, and free water, as well as the content of calciumhydroxide, have been determined from quantification of the water evolved by thermal analysis. Application of this combination of methods demonstrates that the cement paste structure can be changed markedly by addition of non-pozzolanic clays. In particular, the addition of smectite or palygorskite leads to pastes having increased amount of interconnected fine pores which in the corresponding mortars are connected to the ITZ.

## 2. Experimental investigations

### 2.1. Materials

A white Portland cement from Aalborg Portland A/S, Denmark, and distilled water were used for all samples. The bulk oxide composition of the cement is: 68.3 wt.% CaO, 25.0 wt.% $SiO_2$, 1.87 wt.% $Al_2O_3$, 0.45 wt.% $Fe_2O_3$, 0.68 wt.% MgO, 0.01 wt.% $TiO_2$, 0.01 wt.% MnO, 0.17 wt.% $Na_2O$, 0.07 wt.% $K_2O$, and 0.16 wt.% $P_2O_5$. The silica fume was dry powder from Elkem Materials, Norway. Palygorskite, a needle shaped 2:1 layer mineral (Fig. 1a), was obtained from Tolsa, Spain and consists of particles having a diameter of 0.1 μm and a length of several μm and with a specific surface area of 112 $m^2/g$ determined from nitrogen adsorption. Kaolinite was provided by Imery, UK, and consists of platy particles having approx. equal width and thickness (0.005–0.05 μm) (Fig. 1b) and a specific surface area of 19 $m^2/g$. Bentonite is a raw material dominated by the clay mineral smectite. The bentonite (smectite) from Leca, Denmark, consists of flexible laths having the average dimensions: thickness 0.003 μm, width ~0.1 μm, length 0.1–0.5 μm (Fig. 1c), and a specific surface area of 79 $m^2/g$ determined by nitrogen adsorption.

Paste samples were prepared with w/c ratios 0.40 and 0.50. The mortar samples were prepared with seasand (0–2 mm, Class E from RN Sten & Grus, Denmark) and contained 40% sand by volume. The compositions of the different mixtures for the pastes and mortars are summarized in Table 1a and 1b, respectively. Reference samples of pure Portland cement and samples with addition of kaolinite, bentonite, palygorskite and silica fume added in an amount of 10% by weight (wt.%) of the solid (cement and additive) were prepared. Additional water was added to the palygorskite paste assuming a palygorskite adsorption of 373 wt.% water, and to the bentonite mixes assuming a bentonite water adsorption of 193 wt.%. These adsorption values were estimated in the following way: the clay was suspended in a 1.0 M $CaCl_2$ solution having a high ionic strength of $Ca^{2+}$ ions and thus a high flocculation effect. The suspended clay was repeatedly stirred and centrifuged to constant weight and the amount of water adsorbed was determined by weight. Silica fume was added as a dry powder and the layer silicates as suspensions. In the preparation of the samples, the dispersion of the layer silicates in the mixtures was carefully considered. Bleeding was not observed except a faint bleeding for the reference and palygorskite pastes having w/c 0.50. Samples were stored in closed plastic containers, which were kept in a water saturated atmosphere at room temperature to limit long term evaporation and carbonation reactions.

### 2.2. Methods

#### 2.2.1. Atomic force microscopy

AFM was carried out on a Rasterscope 4000 instrument with the tip running in non-contact mode and with an applied force of 0.1 or 0.15 nN at room temperature and normal humidity (40–60% RH). However, the bentonite was scanned in contact mode with applied force 1 nN. Fractured surfaces of pieces of paste were scanned for 6 h at room conditions (40–60% RH). During night the specimens were stored at 100% humidity, and were discarded after maximum 3 days. The clay specimens for the AFM measurements were prepared by letting a drop of suspended clay dry on a block of highly

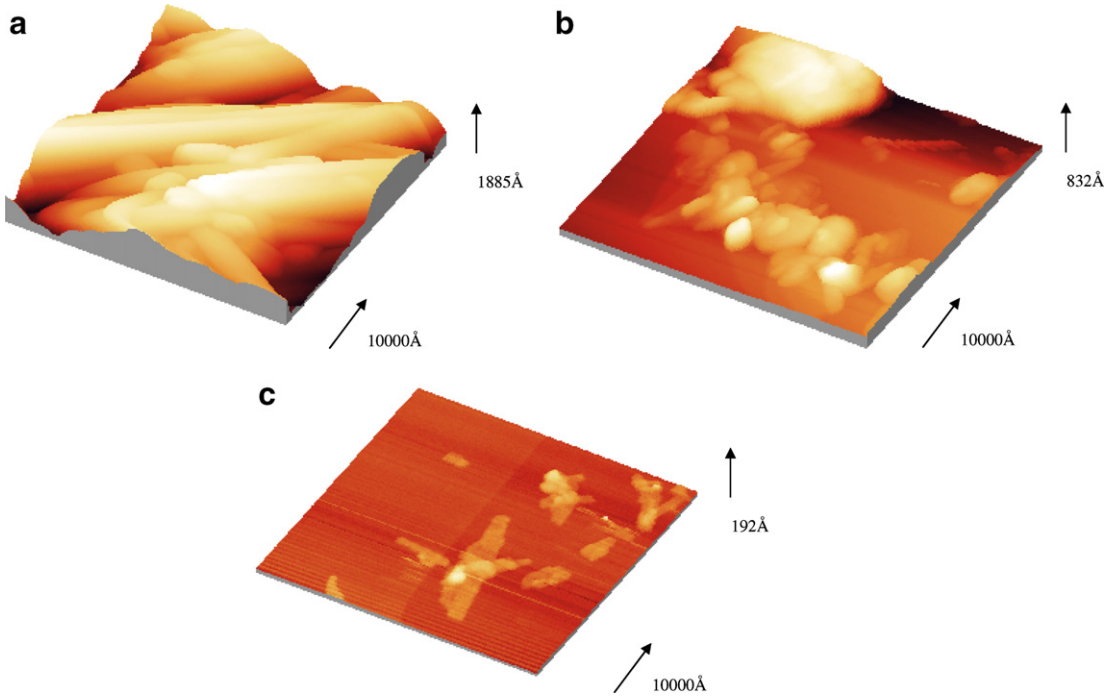


**Fig. 1.** Atomic force microscope images of the raw clays (a) palygorskite, (b) kaolinite, and (c) bentonite, used as additives in the cement mixtures. Particles dispersed and deposited on highly oriented pyrolytic graphite. For each image is shown lateral distances and vertical distance (colours from black to white correspond to the vertical scale).

**Table 1a**
Compositions of the paste mixtures (weight ratios and percentages)

| | w(f)/c | (w(f) + w(a))/c | (w(f) + w(a))/s | Water (%) | Cement (%) | Additive (%) |
|---|---|---|---|---|---|---|
| Kaolinite | 0.40 | 0.40 | 0.36 | 26.47 | 66.18 | 7.35 |
| | 0.50 | 0.50 | 0.45 | 31.04 | 62.07 | 6.89 |
| Palygorskite | 0.40 | 0.81 | 0.73 | 42.29 | 51.95 | 5.77 |
| | 0.50 | 0.91 | 0.82 | 45.14 | 49.38 | 5.48 |
| Bentonite | 0.40 | 0.61 | 0.55 | 35.59 | 57.97 | 6.43 |
| | 0.50 | 0.71 | 0.64 | 39.12 | 54.79 | 6.08 |
| Silica fume | 0.40 | 0.40 | 0.36 | 26.47 | 66.18 | 7.35 |
| | 0.50 | 0.50 | 0.45 | 31.04 | 62.07 | 6.89 |
| Reference | 0.40 | 0.40 | 0.40 | 28.57 | 71.43 | 0.00 |
| | 0.50 | 0.50 | 0.50 | 33.33 | 66.67 | 0.00 |

w(f), free water; w(a), water adsorbed in additives.

**Table 1b**
Compositions of the mortars

| | w(f)/c | Water (%) | Cement (%) | Additive (%) | Sand (%) |
|---|---|---|---|---|---|
| Kaolinite | 0.40 | 15.88 | 39.71 | 4.41 | 40 |
| | 0.50 | 18.62 | 37.24 | 4.13 | 40 |
| Palygorskite | 0.40 | 25.37 | 31.17 | 3.46 | 40 |
| | 0.50 | 27.08 | 29.63 | 3.29 | 40 |
| Bentonite | 0.40 | 21.36 | 34.78 | 3.86 | 40 |
| | 0.50 | 23.47 | 32.88 | 3.65 | 40 |
| Silica fume | 0.40 | 15.88 | 39.71 | 4.41 | 40 |
| | 0.50 | 18.62 | 37.24 | 4.13 | 40 |
| Reference | 0.40 | 17.14 | 42.86 | 0.00 | 40 |
| | 0.50 | 20.00 | 40.00 | 0.00 | 40 |

Weight ratios and percentages, except for the amount of added sand, which is given in volume percent.

oriented pyrolytic graphite. Several (~20) images, 1 μm by 1 μm, were scanned at different places for each specimen. However, the small area of each image, while providing high resolution of the surface in three dimensions, makes it difficult to obtain a representative imaging of the total sample at the same time, as compared to e.g. scanning electron microscope images.

*2.2.2. Thermal analysis of paste samples*

The amount of evaporable water was determined by heating samples ground to <2 mm to constant weight at 105 °C. Thermal analysis (DTA) with infrared detection of evolved water (EWA) and carbondioxide was carried out on powdered samples in a Stanton–Redcroft system [21] The gas flow was 400 ml $N_2$/min and the heating rate was 10 °C/min. Prior to heating, the samples were dried at room temperature with the gas flow of pure nitrogen in the DTA instrument until water release ceased (see e.g. [22]). The powdered samples were prepared by grinding by hand immediately before analysis. It should be noted that the peak temperatures do not reflect reaction temperatures but temperatures of highest reaction rate.

Non-evaporable water [4] was determined from the evolved water curve for samples previously outgassed in high vacuum for 3–5 days at 22 °C until stable vacuum was achieved (Fig. 2a). The total amount of non-evaporable water (including that from calciumhydroxide) was determined from the water release in the range 105–700 °C (the water release stopped at this temperature). In addition the non-evaporable water corresponding to the broad peak for evolved water at 105–200 °C (in these samples at ~180 °C) was determined.

The amount of non-evaporable water corresponding to the peak at ~180 °C plus the amount of physically adsorbed water was determined for fresh samples from the peak for evolved water (in these samples at ~130 °C) (Fig. 2b). The amount of physically adsorbed water was calculated from this quantity by subtraction of the amount of non-evaporable water due to the peak at ~180 °C in outgassed samples (Fig. 2a).

The amount of calcium hydroxide was calculated from the evolved water peak at 500–550 °C.

*2.2.3. Gas porosimetry*

*2.2.3.1. Pore system and adsorbents.* The spatial dimensions for the He, $N_2$, and $H_2O$ atoms/molecules can roughly be approximated by a sphere with a radius of 0.93 Å (He), a cylinder with a radius

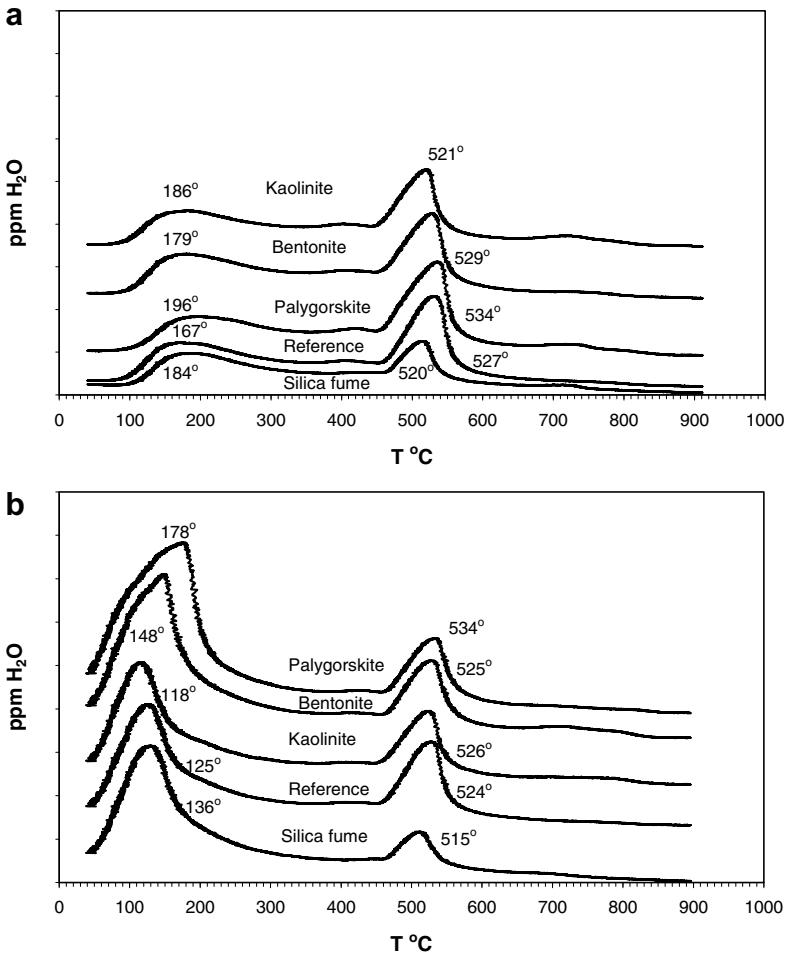


**Fig. 2.** Curves for the evolved water from thermal analysis for the pastes with w/c = 0.4 and hydrated for 20 months. The powders were analysed with a heating rate of 10 °C/min, a gas flow of 400 ml $N_2$/min. (a) Pastes previously outgassed at high vacuum and (b) fresh pastes.

of 1.5 Å and a height of 4.1 Å ($N_2$), and a box with dimensions 1.3 Å × 1.5 Å × 2.0 Å ($H_2O$). Furthermore, it is noted that the $H_2O$ molecule exhibits a permanent dipole moment. For dry samples, He porosimetry measures the total open porosity including the very fine pores and pores with very fine inlet constrictions, since the He atom is small, and the measurements are carried out at room temperature, which favours activated diffusion through very fine inlets [23]. The $N_2$ molecule is larger than He and the low temperature for nitrogen adsorption (~77 K) is less favourable for activated entry. Accordingly, the finest pores and pores with very fine inlet constrictions are not included in the nitrogen adsorption measurements. Furthermore, when comparing data on porosity the method of conditioning the sample should be taken into consideration.

*2.2.3.2. Nitrogen adsorption.* Nitrogen adsorption was carried out on a Micromeritics Accusorb instrument. Helium was used for dead-space determination. Samples were crushed and pieces of 1–4 mm diameter used for measurement. Outgassing was performed in high-vacuum (<$10^{-4}$ mm Hg) at 20 °C, in order to minimize drying effects. Outgassing was carried out until stable vacuum was achieved (usually after 3 days). The specific surface area ($S_w$) was calculated from the adsorption isotherm using the BET equation. The volume of pores having a diameter <200 Å was calculated from the amount of nitrogen adsorbed at $p/p_0 = 0.9$, the so-called Gurvitsch porosity [24]. Assuming cylindrical pores the average diameter of pores <200 Å was calculated from the specific surface area and the Gurvitsch porosity. Two sets of samples were investigated after hydration periods of 3 and 17–20 months. In addition, one set of samples hydrated for 12 months was subjected to stepwise dehydration in a desiccator over salt solutions and finally stored over silica gel for 1–3 months in order to investigate the effect of prolonged drying at room temperature and at non-vacuum conditions.

*2.2.3.3. He-porosity and grain density.* He-porosity was determined for samples dried at 110 °C for 2 days or more. The analyses were performed in a temperature controlled laboratory according to guidelines published by the American Petroleum Institute [25]. The sample grain volume (or solid matrix volume) was measured on dried samples in a Boyle's Law double cell helium porosimeter. Sample bulk volume was measured by submersion of the sample in a mercury bath and calculated using Archimedes principle. The sample pore volume was calculated by subtraction of the grain volume from the bulk volume. The helium porosimeter was calibrated using a set of reference steel plugs before the samples were measured. The samples used for these measurements were plugs drilled from the cylinders of hydrated paste and mortar. Sample grain density (or matrix density) was calculated from the grain volume measurement and the weight of the dried sample. The precision expressed as a standard deviation is 0.1 porosity percent on the

He-porosity determination for sample porosities >1%, and 0.003 g/cc on the sample grain density.

*2.2.4. Low-temperature microcalorimetry*

The samples were saturated prior to testing according to [26]. Excess liquid was removed with a damp cloth. After the low-temperature microcalorimetry (LTC) measurement, the samples were dried at 105 ± 5 °C until constant weight was achieved (±0.1 °C). The LTC measurements were performed in a low-temperature Calvet Micro Calorimeter, model "−196–200 °C", from Setaram [27,28]. Temperature cycles were made between + 20 °C and minimum −48 °C. The cooling and heating rates were −3.3 °C/h and +4.1 °C/h, respectively. No nucleation agent was used. The heat flow is given as the apparent heat capacity calculated using the method of Sellevold and Bager [29]. The measured temperatures are registered in the reference block. The cylindrical test samples of cement paste and mortar have a diameter of 15 mm and a length of 70 mm.

*2.2.5. Water desorption*

Cylinders of paste (2.5 cm diameter, length 2.5 cm) and mortar (4 cm diameter, length 4 cm) were placed in desiccators and weighed after 1 week. The first step was in a desiccator with water, then with the following saturated salt solutions: $K_2SO_4$ (97% RH); $KNO_3$ (93% RH); KCl (86% RH); NaCl (75% RH); NaBr (59% RH); $MgCl_2$ (33% RH); K-acetate (23% RH); LiCl (12% RH); and finally in a desiccator over silica gel for 1–3 months. Each cylinder was carried through the succession of humidity controls.

*2.2.6. Comment on mercury intrusion porosimetry*

It has been customary to use mercury intrusion porosimetry (MIP) to evaluate pore-size distributions in cementitious materials. However, pores with a diameter of <30 Å are normally not intruded. High pressure is needed to intrude the fine pores, and the pressures of MIP may actually damage the structure of cementitious materials [30]. Furthermore, pore-size distributions from MIP do not reflect the sizes of the pores that actually exist in these systems, because only intrusion threshold parameters and intrudable pore space are measured [31]. For these reasons, MIP was not applied in the present investigation. In the present study, freezing curves obtained by LTC are applied for assessment of percolated pore sizes. In contrast to MIP, LTC does not require drying of the samples prior to testing.

## 3. Results and discussion

*3.1. Structural changes due to drying and storage*

The structure of cementitious materials changes during water desorption, e.g., as illustrated by data on the surface area [3]. Thus, the method of drying the samples prior to gas adsorption and porosity investigations influences the structure.

In order to compare the effect of drying in vacuum, as used for nitrogen adsorption, and the effect of oven-drying used for helium porosimetry and density determination, one paste sample (reference w/c 0.4, 12 months hydration) was divided into two parts, where one part was exposed to vacuum drying while the other part was dried in an oven at 105 °C. For each of these parts nitrogen adsorption was subsequently carried out. The specific surface area, derived from these measurements, is 41 $m^2/g$ for the vacuum-dried sample and 80 $m^2/g$ for the oven-dried sample. However, the adsorption isotherms have almost identical shape (Fig. 3) indicating no change in the pore-size distribution. This indicates that the oven-drying has widened the gel-pore interconnections in the pore system without any other significant changes in the pore structure. Similarly, Lion et al. [32] found increases in porosity and gas permeability, which could be assigned to pore widening after heating. However, Gran and Hansen [33] found that drying at 105 °C reduces the specific surface area measured by $^1H$ NMR and attributed this to a coarsening of the pore structure, while Juenger and Jennings [3] found that oven drying relative to D-drying (dry-ice drying) causes a decrease in surface area, as measured with nitrogen, and assigned this to drying shrinkage of the LD C–S–H.

The drying time is, in addition to exposure conditions (relative humidity and temperature), very important for the structure of cementitious materials. For example, it has been observed that prolonged drying decreases the surface area [34,35]. Samples are dried prior to adsorption, e.g., by D-drying for periods as long as 3 weeks [17]. Rarick et al. [35] found that the nitrogen surface area of Portland cement paste decreased with storage time after D-drying which they tentatively attributed to carbonation. In the present investigation, however, the drying of samples for long time for water desorption took place in desiccators and thermal analysis has shown that there are no measurable amounts of carbonates in the reference paste samples after this drying procedure. In the present investigation, pastes from the 2 months stepwise water desorption and subsequently 1–3 months storage over silica gel (Table 2, "12 months, desic.") have a much lower specific surface area and pore volume determined by nitrogen as compared to the previously non-dried ("fresh") pastes (i.e., "3" and "17–20 months" in Table 2) (see Fig. 4a and b). The average pore size is larger for the pastes dried over silica gel (Table 2). This agrees with the results of Lawrence et al. (see [4]), who found that pastes having been rapidly dried (such as those only being outgassed at high vacuum in the present investigation) were likely to be closest in structure to undried pastes. It should be noted that both these samples and the fresh pastes were outgassed in high vacuum at 20 °C for 4 days and that this outgassing resulted in a removal of so much water that no extra water was removed by a subsequent heating at 110 °C.

Similarly for the mortars the prolonged drying over silica gel has caused a strong decrease in both specific surface area and Gurvitsch porosity as compared to the previously non-dried (fresh) mortars investigated after 3 months of hydration (Table 3).

The influence of drying and subsequent storage should be kept in mind when interpreting porosity data; e.g. water desorption curves will reflect a series of structures representing different states during drying. In mortars and dense pastes, the capillary system can consist of capillary pores, interconnected solely by gel pores [31]. This system results in the "ink bottle" effect, e.g., as observed by MIP, LTC and nitrogen adsorption measurements [36,37].

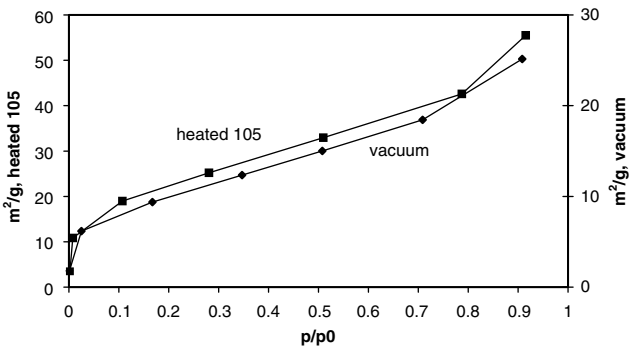


**Fig. 3.** Nitrogen adsorption isotherm for the reference paste, w/c = 0.4 and hydrated for one year, after outgassing in vacuum (vertical scale to the right) and after heating at 105 °C (vertical scale to the left).

**Table 2**
Nitrogen adsorption data for the paste samples: specific surface area ($S_w$), Gurvitsch pore volumes and average pore diameter

| Paste | w/c | 3 months | | | 17–20 months | | | 12 months, desic. | | |
|---|---|---|---|---|---|---|---|---|---|---|
| | | $S_w$ ($m^2$/g) | Pores (vol $cm^3$/g) | Diameter (Å) | $S_w$ ($m^2$/g) | Pores (vol $cm^3$/g) | Diameter (Å) | $S_w$ ($m^2$/g) | Pores (vol $cm^3$/g) | Diameter (Å) |
| Kaolinite | 0.40 | 26 | 0.034 | 23 | 46 | 0.049 | 21 | | | |
| | 0.50 | 59 | 0.085 | 24 | 80 | 0.082 | 21 | | | |
| Palygorskite | 0.40 | 75 | 0.126 | 23 | 128 | | | 25 | 0.044 | 35 |
| | 0.50 | 107 | 0.144 | 20 | | | | | | |
| Bentonite | 0.40 | 64 | 0.095 | 23 | 112 | 0.121 | 22 | 13 | 0.026 | 40 |
| | 0.50 | 99 | 0.140 | 21 | 112 | 0.124 | 22 | 21 | 0.033 | 31 |
| Silica fume | 0.40 | 14 | 0.025 | 29 | 10 | 0.014 | 30 | | | |
| | 0.50 | 33 | 0.054 | 27 | 30 | 0.037 | 24 | 10 | 0.015 | 30 |
| Reference | 0.40 | 59 | 0.068 | 19 | 59 | 0.064 | 22 | 7 | 0.013 | 37 |
| | 0.50 | 84 | 0.095 | 20 | 90 | 0.086 | 20 | 10 | 0.018 | 36 |

Specific surface area and the pore volumes are per g dry sample.

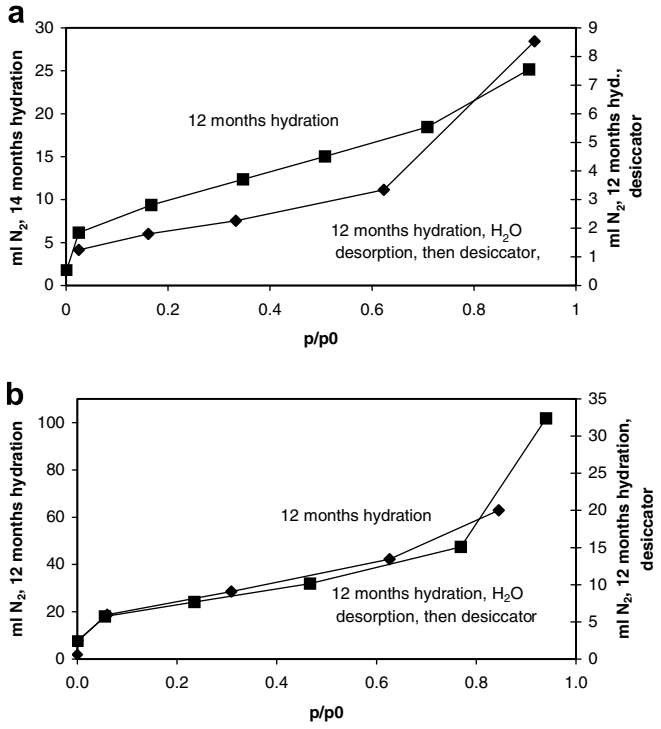


**Fig. 4.** Nitrogen adsorption isotherms for pastes with w/c = 0.4 hydrated for one year, and after outgassing in vacuum (vertical scale to the right) and after water desorption and storage over silica gel (vertical scale to the left). (a) The reference paste and (b) the palygorskite paste.

### *3.2. DTA-evolved water analysis: calcium hydroxide content, structure and porosity*

The amount of non-evaporable water [4] released at 105–700 °C is low for the silica fume paste with w/c = 0.4, somewhat larger for the kaolinite pastes, and largest for the reference, bentonite, and the palygorskite pastes and for the silica fume paste with w/c = 0.5 (Table 4, Fig. 2a). The amount of non-evaporable water released in the reaction at ~180 °C (the interval 105–400 °C) is 4.7–6.5% for all pastes, and it does not change for the w/c ratios of 0.4 and 0.5. Stepkowska et al. [38] assigned this release (110–400 °C) to water from the C–S–H and other hydrates and found values of 5.4% and 7.6% for two Portland cement pastes having w/c 0.4 and an age of five years.

For the physically adsorbed water Stepkowska et al. [38] found a release of 7.9% and 7.8% at 150 and 160 °C, respectively, for the two pastes. In the present investigation, the amount of physically adsorbed water increases on going from w/c = 0.4 to w/c = 0.5 and the amount is similar for the reference and kaolinite pastes, but larger for the bentonite, silica fume and especially the palygorskite pastes (Table 4). The rather narrow release of physically adsorbed water at ~100 °C (Fig. 2b) resembles the release of physically adsorbed water from the layers of clays [39]. In fact, the water release observed as a rather narrow peak in DTA measurements at 90–105 °C was demonstrated by Feldman and Ramachandran [40] to be interlayer water in the layered structure of the C–S–H, the water adsorbed physically on the outer surfaces being released at 65–80 °C [40]. This peak is absent in the EWA curves (Fig. 2b) of the present investigation, probably because the sample powder prior to heating was conditioned in the DTA apparatus in a gas flow of dry nitrogen. Feldman [41] estimated the interlayer spacing in the C–S–H to be ~3 Å in thickness, and the layers are thus only about one molecule of water apart.

**Table 3**
Nitrogen adsorption data for the mortar samples: specific surface area ($S_w$) and pore volumes

| Mortar | w/c | 3 months | | 12 months, desic. | |
|---|---|---|---|---|---|
| | | $S_w$ ($m^2$/g) | Pores ($cm^3$/g) | $S_w$ ($m^2$/g) | Pores ($cm^3$/g) |
| Kaolinite | 0.40 | 36 | 0.044 | 10 | 0.016 |
| | 0.50 | 55 | 0.066 | 27 | 0.028 |
| Palygorskite | 0.40 | 91 | 0.088 | 17 | |
| | 0.50 | 94 | 0.130 | 23 | 0.035 |
| Bentonite | 0.40 | 61 | 0.076 | 13 | 0.019 |
| | 0.50 | 73 | | 15 | 0.027 |
| Silica fume | 0.40 | 36 | 0.042 | 6 | |
| | 0.50 | 14 | 0.026 | 8 | 0.014 |
| Reference | 0.40 | 44 | 0.046 | 12 | 0.016 |
| | 0.50 | 41 | 0.052 | 17 | 0.025 |

Specific surface area and the pore volumes are per g dry sample.

The amount of evaporable water also increases when the w/c is changed from 0.4 to 0.5 (Table 4). Moreover, the amount of evaporable water exhibits almost the same variation as the non-evaporable water released at 105–700 °C in that it is similar for the kaolinite and silica fume pastes, larger for the reference pastes, and largest for the palygorskite and bentonite pastes. It is important to note that the evaporable water is determined on samples <2 mm in size, i.e., some of the larger pores may have been destroyed by grinding.

The amount of calcium hydroxide after 3 months of hydration is lowest for the silica fume pastes, followed by the kaolinite paste and is largest for the reference, bentonite and palygorskite pastes (Table 5, Fig. 2a and b). It increases on going from w/c = 0.4 to w/c = 0.5, probably due to an increased degree of hydration at higher w/c. However, this is not confirmed by the present measurements of water release in the temperature range 105–700 °C. The low calcium hydroxide content in the silica fume pastes can be explained

**Table 4**
Results from the DTA-evolved water analysis of pastes: Calculated data for the non-evaporable, physically adsorbed and evaporable water in the C–S–H for the pastes hydrated for 17–20 months

| Paste | w/c | Evaporable[a] | Non-evaporable | | Physically adsorbed Peak ~130 °C |
|---|---|---|---|---|---|
| | | | 105–700 °C | Peak ~180 °C | |
| Kaolinite | 0.40 | 16.1 | 16 | 4.8 | 11 |
| | 0.50 | 21.0 | 15 | 4.7 | 15 |
| Palygorskite | 0.40 | 40.4 | 20 | 5.8 | 29 |
| Bentonite | 0.40 | 30.0 | 20 | 5.9 | 19 |
| | 0.50 | 33.0 | 20 | 4.7 | 24 |
| Silica fume | 0.40 | 20.7 | 13 | 5.5 | 15 |
| | 0.50 | 25.3 | 19 | 6.5 | 18 |
| Reference | 0.40 | 18.2 | 19 | 5.7 | 11 |
| | 0.50 | 22.2 | 18 | 5.8 | 12 |

% of weight of the material heated to 105 °C.
[a] By heating to 105 °C.

by pozzolanic reactions, and this is supported by an observed decrease in the calcium hydroxide to C–S–H ratio for the silica fume samples. The higher calcium hydroxide content in the bentonite, palygorskite and reference pastes compared to the kaolinite pastes can partly be explained by a higher degree of hydration in the bentonite, palygorskite and reference pastes, since the clay minerals exhibit no pozzolanic effects. The amount of calcium hydroxide decreases from 3 months to 17–20 months for the reference pastes, the w/c 0.5 bentonite paste and the w/c 0.4 silica fume paste, whereas it is almost invariant for the other pastes. This may be compared to reported observations of a maximum in calcium hydroxide content for cements high in belite and the fact that the calcium hydroxide content may decrease slightly after 28–91 days even for modern cements high in alite [4].

Based on the non-evaporable water contents (Table 6), Bogue calculation of the clinker minerals [4], and assuming (i) the following non-evaporable water contents for the fully hydrated clinker minerals of 0.24, 0.21, 0.40, and 0.37 (g water)/(g clinker mineral) for $C_3S$, $C_2S$, $C_3A$, and $C_4AF$ [42], respectively, and (ii) simultaneous hydration of all clinker minerals, the degrees of hydration (weighted average) for the 17–20 months old pastes are estimated to be 0.9 or more. The only exception is the paste including kaolinite, for which a lower degree of hydration of 0.8 was achieved. This finding for the kaolinite mixture is in contradiction with the degrees of hydration for alite (>0.95) and belite (>0.85) determined from $^{29}$Si MAS NMR for two similar mixtures of kaolinite and bentonite with white Portland cement (w/c = 0.5) hydrated for one year [15]. The $^{29}$Si and $^{27}$Al MAS NMR investigations of these mixtures give no indications of a lower degree of reactivity for the cement in the kaolinite mixtures. Thus, we expect that the slightly lower degree of hydration, estimated from the non-evaporable water contents for the kaolinite mixture, is due to the approximations used in the calculation of the degree of hydration by this approach.

**Table 5**
Calcium hydroxide content (% of dry material) determined for the paste samples from DTA-evolved water measurements

| | w/c | 3 months hydration | 17–20 months hydration |
|---|---|---|---|
| Kaolinite | 0.40 | 20 | 19 |
| | 0.50 | 23 | 23 |
| Palygorskite | 0.40 | 29 | 30 |
| Bentonite | 0.40 | 23 | 24 |
| | 0.50 | 32 | 25 |
| Silica fume | 0.40 | 13 | 10 |
| | 0.50 | 17 | 16 |
| Reference | 0.40 | 29 | 22 |
| | 0.50 | 32 | 25 |

### 3.3. Microstructure from atomic force microscopy

A transmission electron microscopy (TEM) investigation [43] of a paste made from a mixture of calcium oxide and silica identified a C–S–H interlayered with calcium hydroxide in a lamellar structure with a lamellae thickness of ~10 nm. Moreover, TEM investigations of white Portland cement pastes hydrated for 1–8 years at 20 °C [2,44] have shown that the C–S–H formed inside the original cement grains (the inner product, IP) consists of small, globular particles with a diameter of 4–8 nm. The C–S–H formed in the pore space (the outer product, OP) appears in alite and belite pastes to consist of aggregations of long, thin, fibrillar particles, which in cements blended with slag, metakaolin, or silica fume changes from fibrillar to a foil-like morphology [2].

AFM images of pastes hydrated for 20 months (Figs. 5–9) show globular grains and irregularly shaped pores. The grains are rather small (~100 nm diameter) in the bentonite paste (Fig. 8), larger in the palygorskite (Fig. 9) and kaolinite (Fig. 7) pastes and largest in the reference (Fig. 5) and silica fume (Fig. 6) pastes. In the palygorskite pastes, some large grains are elongated (Fig. 9c). Clay particles could not be observed, probably because cement hydration products have crystallised on the surface of the clay particles.

For all five pastes, the AFM images of the pores demonstrate that calculations assuming the cylindrical pore systems in cement pastes are principally wrong. The layer structure observed in the reference paste (Fig. 5b) resembles the layer structure of clays and conform with the layer structure model for C–S–H. However, the observed layer structure appears to have formed in the pore space. The C–S–H phase formed on the surface of cement grains or of layer silicates may have a quite different structure, as indicated by the AFM images of the kaolinite, bentonite, and palygorskite pastes, and from the 5 nm blades observed for the kaolinite paste (Fig. 7b and c). These blades may well be the C–S–H formed on the kaolinite surfaces and resemble the curved layers of the Feldman–Serada model [6]. Furthermore, they are similar to the foils growing in the pore space observed by TEM [2]. The small 4–8 nm sized globules, observed by TEM and growing on the cement grains, have not been observed by AFM. However, TEM specimens are subjected to elevated temperature and high vacuum, whereas the AFM specimens are scanned at room conditions.

### 3.4. Pore structure of pastes

#### 3.4.1. Specific surface area and porosity from nitrogen adsorption

Nitrogen adsorption isotherms are of the types II or IV of the BET classification, types II and IV being characterized by high (>30) BET surface affinity coefficients [24]. Accordingly, the specific surface areas can be calculated from the linear BET plots [24]. The

**Table 6**
He-porosity (%) of the paste and mortar samples after 3 months of hydration

| | w/c | Pastes | Mortars |
|---|---|---|---|
| Kaolinite | 0.40 | 20.6 | 17.9 |
| | 0.50 | 26.7 | – |
| Palygorskite | 0.40 | 42.4 | 35.1 |
| | 0.50 | 40.6 | 34.1 |
| Bentonite | 0.40 | 34.2 | 25.9 |
| | 0.50 | 39.6 | 30.1 |
| Silica fume | 0.40 | | 13.6 |
| | 0.50 | 22.0 | 17.3 |
| Reference | 0.40 | 20.2 | 17.3 |
| | 0.50 | 25.8 | 19.5 |

The samples were dried at 110 °C prior to the He porosity measurements.

magnitude of the $S_w$ values for pastes (Table 2) corresponds to the values found by Bodor et al. [45] ($S_w$ 53 $m^2/g$ for w/c = 0.4 and $S_w$ = 89 $m^2/g$ for w/c = 0.5). However, the $S_w$ values vary much with drying and preparation techniques (vide supra). Thus, the present discussion of the $S_w$ values will be based on the variations of $S$ with w/c, aggregate, clay, and silica fume addition employed for the studied samples.

Relative to the reference pastes, the silica fume pastes have a lower specific surface area and pore volume. The kaolinite pastes have about the same and the bentonite and palygorskite pastes significantly higher specific surface area and pore volume relative to the reference pastes. Except for the bentonite paste at age 17–20 months, the specific surface areas and the Gurvitsch porosity increase with increase in w/c from 0.4 to 0.5 (Table 2). A constant specific surface area and pore volume is observed for the reference pastes and for the silica fume pastes hydrated for 3–17 months, whereas an increase in specific surface area of 33–100% in the same period of hydration is apparent for the clay pastes. These changes caused by clay addition cannot be due to the specific surface of the clay because the clay surfaces appear according to AFM to be covered with hydration products, as also indicated by kinetic studies of the C–S–H formation for cement–clay mixtures by $^{29}Si$ MAS NMR [15]. Furthermore, addition of e.g. 10% of palygorskite with a specific surface area of 112 $m^2/g$ can at maximum contribute with a specific surface area of 11 $m^2/g$. It is noted that for w/c = 0.4 the increase following palygorskite addition is equal to 69 $m^2/g$ relative to the reference samples.

From small angle scattering (SAXS) measurements, the surface area of pastes has been observed to increase to 600 $m^2/g$ during one year of hydration [46]. However, SAXS is probing size scaled of the order of the radiation, which was 0.7 Å. For Portland cement pastes, Odler and Chen [47] found for 1–24 months of hydration that the $S_w(N_2)$ value did not increase with time for w/c = 0.3, but increased 30% for w/c = 0.6 and 100% for w/c = 1.0. For $S_w(H_2O)$, they found for all w/c ratios an increase with time, by 50% for w/c = 0.3 and w/c = 0.6, and by 100% for w/c = 1.0. Moreover, the observed strong increase in nitrogen adsorption and penetration following heating to 110 °C (Fig. 3) indicates a widening of gel pore connections during heating as mentioned earlier.

For most of the pastes hydrated for 3 or 17–20 months, the average pore diameter calculated from nitrogen adsorption is ~20 Å (Table 2) and this value does not change significantly from 3 to 17 months. An exception is the silica fume paste with w/c = 0.4 where the average pore diameter is ~30 Å.

#### 3.4.2. Helium porosity

The bentonite and palygorskite pastes have high and fairly equal helium porosities (Table 5), which correspond to the experimental and calculated porosities of Portland cement pastes (18 months) by Taylor ([4], Fig. 8.5) except for a small decrease for the palygorskite pastes with increasing w/c ratio from 0.4 to 0.5. The kaolinite, reference and silica fume pastes have equal helium porosities. However, the porosities are only half of the values for the bentonite and palygorskite pastes.

### 3.5. Pore structure of mortars

#### 3.5.1. Specific surface area and porosity from nitrogen adsorption

The specific surface area of mortars with w/c = 0.4 is similar for the reference, kaolinite and silica fume mortars and two to three times larger for the bentonite and palygorskite mortars, largest for the palygorskite mortar (Table 3). This corresponds to the trend found for the pastes. The surface areas increase on going from w/c = 0.4 to w/c = 0.5 for the kaolinite and the bentonite mortars and decrease for the silica fume mortar. The same tendency is seen for the Gurvitsch porosities (Table 3). In accordance with the data for the pastes, the specific surface areas and Gurvitsch porosities decrease strongly following drying over silica gel for 3 months (Table 3).

#### 3.5.2. Helium porosity

The helium porosities for mortar samples with w/c = 0.4 and dried at 110 °C (Table 6) show the same changes with clay addition as the values for nitrogen specific surface area and Gurvitsch porosity. However, the increase of w/c from 0.4 to 0.5 for the silica fume mortar increases the helium porosity slightly. This may reflect that inlet constrictions in the silica fume mortar with w/c = 0.5 have been opened to helium during heating at 110 °C. Alternatively, the small helium atom is able at room temperature to pass inlet constrictions which are closed to nitrogen at −200 °C.

#### 3.5.3. Water and porosity from low-temperature calorimetry, LTC

In LTC measurements freezing of water probably takes place by propagation of an ice front from the specimen surface [28,48]. This means that ice formation in pores with inlet constrictions depends on ice formation in the constrictions and that water in closed pores will be included in non-freezing water. All LTC data given in the following are derived from single experiments, as repetitions undertaken in connection with earlier work, using the same experimental setup, showed limited variability in the results [49] (a general discussion of the assessment of LTC data is also given in that study). The measured heat flow as a function of temperature is shown in Fig. 10. Sellevold and Bager [29] as well as Fontenay and Sellevold [27] found that the temperature difference between the sample and the reference block is typically between 0.4 °C and 0.8 °C during cooling at −3.3 °C/h and heating at 4.1 °C/h. However,

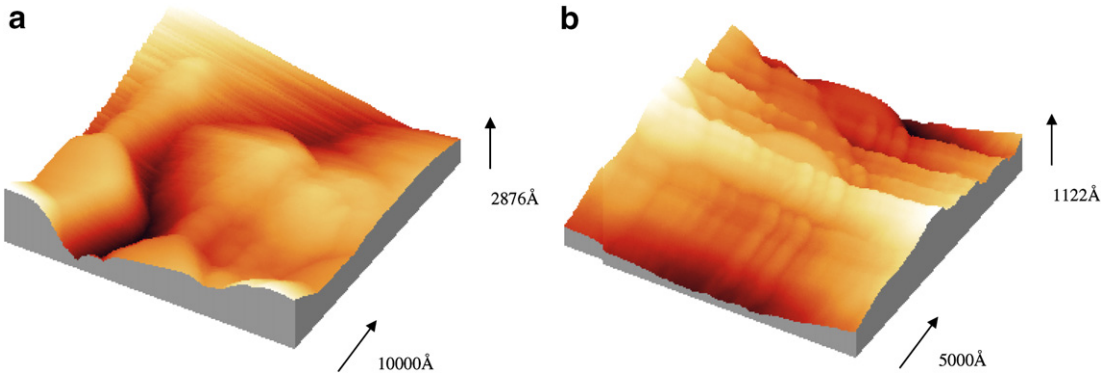


**Fig. 5.** Atomic force microscope images (non-filtered data) of the reference paste (prepared without additives) with w/c = 0.5 and hydrated for 20 months. Freshly fractured surfaces imaged at room conditions. For each image is shown lateral distances and vertical distance (colours from black to white correspond to the vertical scale).

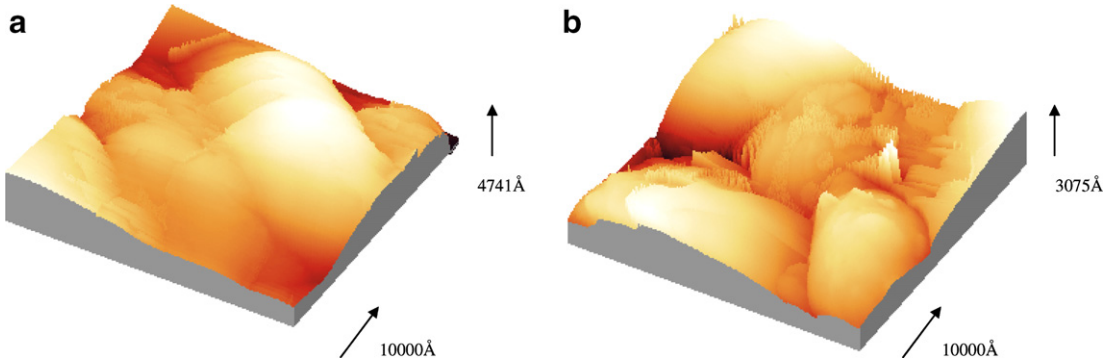


**Fig. 6.** Atomic force microscope images (non-filtered data) of the paste including silica fume hydrated with w/c = 0.5 for 20 months. Freshly fractured surfaces imaged at room conditions. For each image is shown lateral distances and vertical distance (colours from black to white correspond to the vertical scale). The spikes are due to vibrations of the AFM tip.

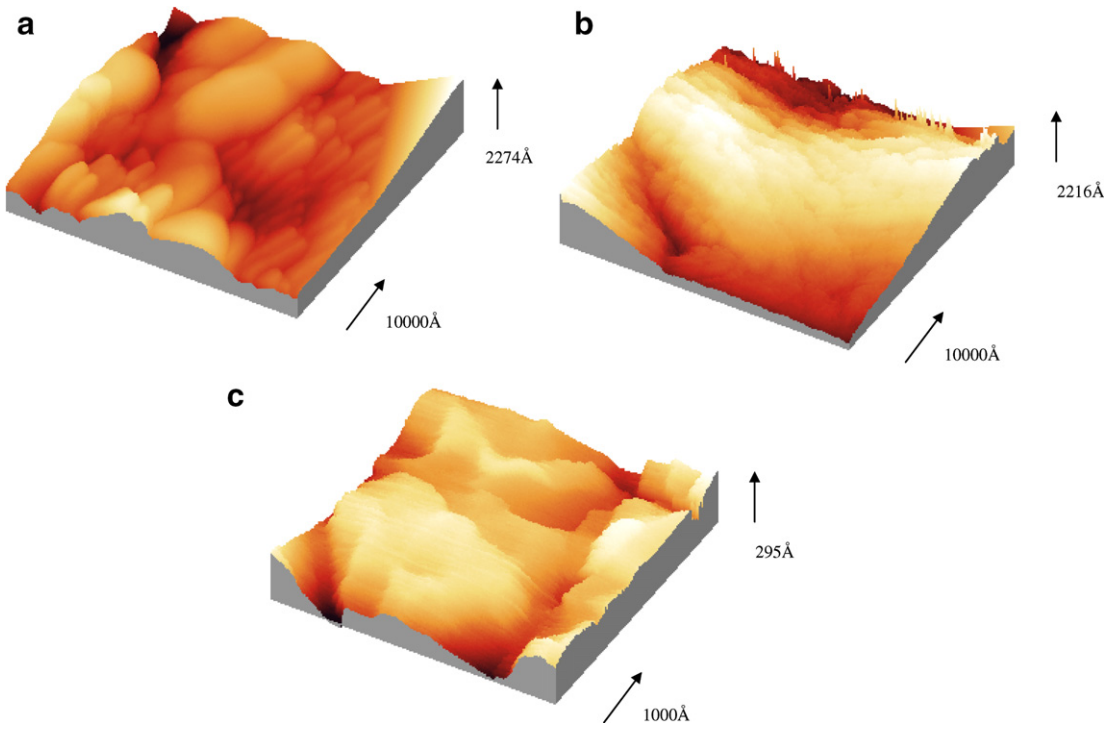


**Fig. 7.** Atomic force microscope images (non-filtered data) of the pastes with addition of kaolinite (w/c = 0.5, 20 months hydration). Freshly fractured surfaces imaged at room conditions. For each image is shown lateral distances and vertical distance (colours from black to white correspond to the vertical scale).

the difference in temperature can be up to several degrees when extensive freezing and thawing take place.

Based on the LTC measurements the ice formed in selected temperature intervals has been calculated using a reported procedure [50] and the results are given in Table 7. Note that ice formation is calculated in the same temperature intervals for all samples and not temperature intervals selected from the positions of each individual peak. The calculated amounts of ice formed are highly influenced by the positioning of the baseline and interpretation should be supported by the graphs.

The amount of evaporable water has been calculated based on the weight of the saturated surface dry sample before LTC and the dried sample after LTC and subsequent drying. The results are given in Table 7. The amount of non-freezable water is calculated as the difference between the amount of evaporable water and freezable water determined by LTC.

In most samples at least three freezing peaks are observed; an initial peak in the temperature interval from 0 to −10 °C, a second peak around −25 °C, and a third peak at approx. −40 °C. Based on the porosity model proposed by Jennings [7], Snyder and Bentz [51] have suggested the interpretation of freezing peaks given in Table 8. In their work they also included data from the studies of Bager and Sellevold [28]. Due to supercooling, ice forms below the normal freezing point. The first freezing peak is assumed to originate from the freezing of "bulk" water, i.e. water in capillary pores connected to the surface as well as possible excess water on the surface of the samples. This peak appears in the temperature interval from 0 to −10 °C.

All samples are observed to have a freezing peak around −25 °C, except for the mixtures with silica fume. This peak is attributed to percolated inter LD and HD C–S–H pores (Table 8). The freezing peak around −40 °C is attributed to interglobular LD C–S–H pores

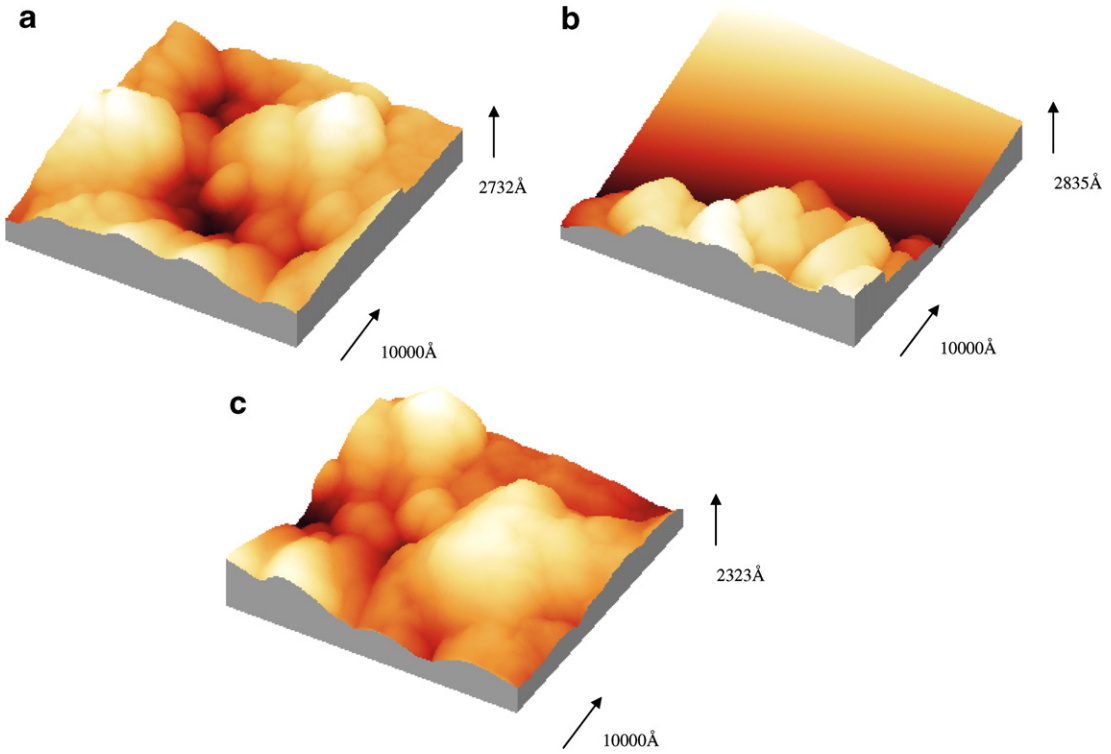


**Fig. 8.** Atomic force microscope images (non-filtered data) of the paste prepared with addition of bentonite (w/c = 0.5, 20 months of hydration). Freshly fractured surfaces imaged at room conditions. For each image is shown lateral distances and vertical distance (colours from black to white correspond to the vertical scale).

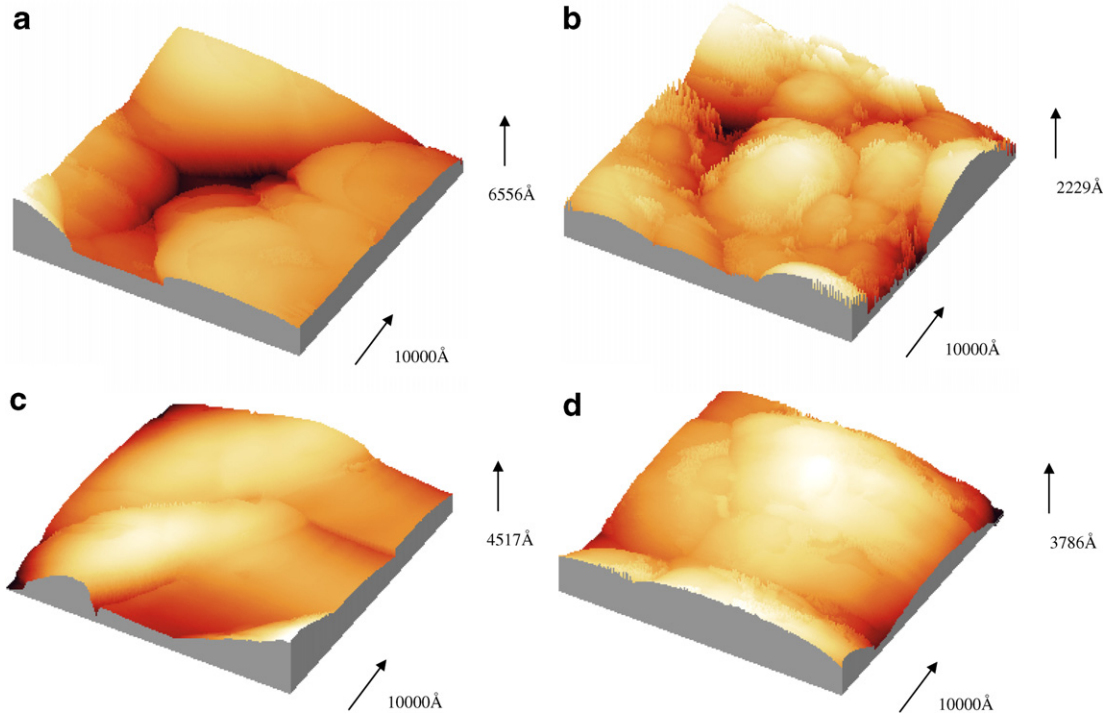


**Fig. 9.** Atomic force microscope images (non-filtered data) of the paste prepared with addition of palygorskite (w/c = 0.4, 20 months of hydration). Freshly fractured surfaces imaged at room conditions. For each image is shown lateral distances and vertical distance (colours from black to white correspond to the vertical scale). The spikes in (b) and (c) are due to vibrations of the AFM tip.

and it is observed for all samples; although only to a small extent for the reference mortar with w/c = 0.4. Some freezing seems to take place between the initial freezing peak and the peak around −25 °C in the bentonite and palygorskite mortars both with w/c = 0.5. However, such freezing is not observed for the bentonite mortar with w/c = 0.4 and the absence of this peak indicates that percolated pores of the size between capillary and inter LD and HD pores are absent in this mortar. Finally, some freezing seems

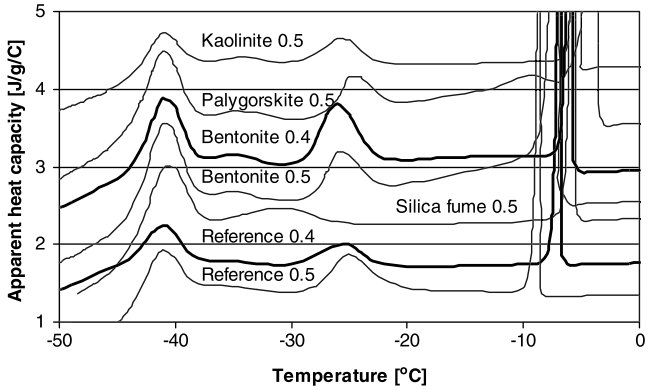


**Fig. 10.** Apparent heat capacity as a function of temperature for pastes with w/c 0.4 (bold) and 0.5. The baselines have been adjusted in order to display all curves in the same graph (i.e., an adjustment of the origin for the abscissa axis).

to take place in the temperature interval from −28 to −38 °C, an effect that is most pronounced for the sample with silica fume, indicating a change in the structure of the C–S–H for this material.

The amount of evaporable water is equal for the reference, silica fume and kaolinite mortars and larger for the palygorskite and bentonite mortars (Table 7). The same tendency is observed for freezable water in (i) capillary pores freezing at 0 to −10 °C, (ii) interconnected gel pores freezing at −10 to −30 °C, (iii) interglobule pores in LD C–S–H freezing at −30 to −40 °C, and for the non-freezable water (Table 7). For all mortars, each type of water increases with the increase in w/c from 0.4 to 0.5. The largest part of the evaporable water is present as non-freezable water.

For the freezeable water, the main part in the silica fume mortar is present in the interglobule pores, whereas for the clay mortars the largest part is present in the capillary pores. For the reference mortar, about equal amounts of freezable water are present in the three types of pores. Thus, relatively to the reference samples the addition of clay has resulted in a large amount of water freezing at temperatures corresponding to capillary pore dimensions, whereas addition of silica fume has created pores corresponding to LD C–S–H interglobular pore dimensions. However, considering the additional nitrogen surface area and helium porosity resulting from the addition of sand (Table 9), it may be concluded that the ITZ of the clay additive mortars is connected to the surface but is closed for the silica fume mortars.

### 3.5.4. The interfacial transition zone

The ITZ may be modified by addition of fine particles. Nano- and micron-sized layer silicates in the ITZ may modify the porosity of this zone due to packing effects and due to dendritic growth of C–S–H at the silicate surface. Furthermore, pore structure modifications in the paste due to these additive materials will change the connection through pores between the ITZ and the surface of the mortar/concrete. In order to investigate this effect the differences between pastes and the corresponding mortars were calculated after 3 months of hydration with respect to specific surface area per gram paste ($\Delta S_w$) and porosity per gram paste (ΔHe) (Table 9).

After hydration for 3 months the $\Delta S_w$ values are larger for w/c = 0.4 than for w/c = 0.5, except for the kaolinite mortars. As the specific surface area ($S_w$) most likely originates from the LD C–S–H, a large amount of LD C–S–H seems to have formed in the ITZ for most mixtures. An alternative explanation is that the proportion of pores in LD C–S–H connected to the surface increases with sand addition, probably because of linkage of otherwise closed pores through the ITZ. This explains that the effect of sand addition is most pronounced for w/c = 0.4. The fact that the $\Delta S_w$ values are negative for silica fume and reference mortars with w/c 0.5 may reflect that HD C–S–H has formed and closed the connections to the ITZ at this w/c ratio. However, the clay additive mortars have a pore system open to $N_2$ and connected to the ITZ. This conforms with the larger amounts of pores seen in LTC of the clay additive mortars (Table 7).

An increase in ΔHe is found for all samples hydrated for 3 months. This indicates that the pore blocking effect observed for $S_w$ values at w/c = 0.4 is not so pronounced for helium. Furthermore, the ΔHe values are roughly similar for w/c = 0.4 and w/c = 0.5. These findings may reflect that helium can penetrate the narrow paste pores blocked for nitrogen and present in large amounts at w/c = 0.4 for all mixtures and at w/c = 0.5 for the reference and silica fume mixtures. However, it is more likely that the structure has opened during heating at 110 °C prior to helium porosity measurements, as found by the specific surface area measurements of the samples before and after heating.

**Table 8**
Suggested interpretation of the peak temperature observed by LTC

| Pore size classes | Temperature interval | | |
|---|---|---|---|
| | Snyder and Bentz [51] | Bager and Sellevold [48] | This work |
| Bulk water | – | – | 0 to −10 °C |
| Percolated capillary pores | −20 | −10 | 0 to −10 °C |
| Percolated inter LD and HD gel pores | −30 | −25 | Around −25 °C |
| Percolated inter globule pores in LD gel | −45 | −45 | Around −40 °C |

**Table 7**
Low-temperature calorimetry (LTC) data for the mortar samples

| | w/c | Evaporable | Freezable | | | Non-freezable |
|---|---|---|---|---|---|---|
| | | | 0 to −10 °C | −10 to −30 °C | −30 to −43 °C | |
| Kaolinite | 0.40 | | | | | |
| | 0.50 | 0.164 | 0.018 | 0.009 | 0.008 | 0.130 |
| Palygorskite | 0.40 | | | | | |
| | 0.50 | 0.277 | 0.043 | 0.024 | 0.007 | 0.202 |
| Bentonite | 0.40 | 0.224 | 0.019 | 0.015 | 0.007 | 0.182 |
| | 0.50 | 0.260 | 0.044 | 0.025 | 0.012 | 0.178 |
| Silica fume | 0.40 | | | | | |
| | 0.50 | 0.191 | 0.019 | 0.003 | 0.029 | 0.140 |
| Reference | 0.40 | 0.149 | 0.009 | −0.004 | −0.002 | 0.146 |
| | 0.50 | 0.190 | 0.011 | 0.012 | 0.014 | 0.154 |

Calculated amounts of evaporable, freezable, and non-freezable water (g/g dry material).

### 3.6. Structural modifications of pastes by clay and silica fume addition

$^{29}$Si MAS NMR studies have demonstrated that the clay minerals kaolinite and smectite (in bentonite) act as nucleation agents for the C–S–H hydration products [15]. Furthermore, it was found that the addition of bentonite resulted in C–S–H with a shorter average chain length of $SiO_4$ tetrahedra, whereas addition of kaolinite resulted in a longer average chain length as compared to hydrated samples of a pure white Portland cement paste. The effect of addition of the clay minerals palygorskite, smectite, and kaolinite is principally different from that of silica fume, since the clay minerals are not pozzolanic and thereby do not dissolve during the cement hydration.

For the silica fume paste, the large grains observed by AFM (Fig. 6a and b) correspond to the relatively low specific surface area and the low volume of fine pores determined with nitrogen adsorption (Table 2). As mentioned earlier, the porosities determined using nitrogen and helium reflect the amount of open pore space. However, the amount of closed pore space in the cylinders that have been investigated by helium porosimetry may be estimated from an evaluation of the grain density values (Table 10). Only the silica fume paste with w/c = 0.5 deviates from the other samples by having a significantly lower grain density. This deviation cannot be explained by a lower density of the grains. Therefore, as the helium porosimetry values for the silica fume mixtures are similar to those of the reference and kaolinite pastes, the lower grain density for the silica fume paste reflects a larger amount of closed pores. The fact that the $S_w$ value for the silica fume paste is much lower than for the other pastes shows that, in addition to these closed pores, the silica fume paste contains a large proportion of pores, which are open to helium but closed to nitrogen. Alternatively, the pores may be opened during the heating at 110 °C prior to helium porosimetry. The closed porosity and inlet constrictions are probably due to the pozzolanic nature of the silica fume, which during hydration may block pores and create closed pore spaces or pore constrictions. This is in accordance with the observation by Bentz et al. [11] that an addition of 10% silica fume results in a reduced diffusion of chloride ions both in the capillary pores and in the C–S–H, and the hypothesis [52] that initially formed $Ca(OH)_2$ crystals may dissolve due to reaction with silica fume and the space be left empty.

For the kaolinite paste, the AFM images (Fig. 7a–e) indicate C–S–H growth on the particle surfaces of kaolinite. Since these particles are large (e.g., compared to the smectite particles, Fig. 8a–d), the resulting structure will be composed of large particles and large interparticle pores. The grain density of the paste with w/c = 0.4 is larger than for the reference paste indicating a smaller amount of closed pores, whereas the paste for w/c = 0.5 hardly deviates from the reference (Table 10). The helium porosities for the kaolinite pastes are similar to those for the reference (Table 6), whereas the $S_w$ values for the kaolinite pastes are significantly lower than those for the reference (Table 2). This indicates that some inlet constrictions have formed. However, these are either penetrable to helium or removed during the heating at 110 °C prior to the helium porosimetry measurements.

**Table 9**
Additional specific surface area, $\Delta S_w$ ($m^2$/g dry paste), and additional He-porosity (ΔHe) created through addition of 40% (by volume) sand to pastes (3 months hydration)

| | w/c | $\Delta S_w$ ($m^2$/g) | ΔHe (%) |
|---|---|---|---|
| Kaolinite | 0.40 | 34 | 9.2 |
| | 0.50 | 33 | |
| Palygorskite | 0.40 | 77 | 16.1 |
| | 0.50 | 50 | 16.2 |
| Bentonite | 0.40 | 38 | 9.0 |
| | 0.50 | 23 | 10.6 |
| Silica fume | 0.40 | 46 | |
| | 0.50 | −10 | 6.8 |
| Reference | 0.40 | 14 | 8.6 |
| | 0.50 | −16 | 6.7 |

**Table 10**
Grain density values (g/$cm^3$) for the samples hydrated for 3 months and dried at 110 °C prior to the measurements

| | w/c | Pastes | Mortars |
|---|---|---|---|
| Kaolinite | 0.40 | 2.20 | 2.35 |
| | 0.50 | 2.13 | |
| Palygorskite | 0.40 | 2.03 | 2.23 |
| | 0.50 | 2.10 | 2.26 |
| Bentonite | 0.40 | 2.05 | 2.26 |
| | 0.50 | 2.08 | 2.25 |
| Silica fume | 0.40 | | 2.24 |
| | 0.50 | 1.94 | 2.17 |
| Reference | 0.40 | 2.11 | 2.29 |
| | 0.50 | 2.09 | 2.24 |

For the bentonite paste, the particles observed in the AFM images (Fig. 8a–d) may have formed by C–S–H growth on the nano-sized smectite particle laths. This growth pattern has formed a paste having a large specific surface area, as measured with nitrogen, and especially a larger volume of fine pores compared to the reference paste which contains larger grains with correspondingly larger pores (Table 2). For the cylinders of the bentonite mixtures, the grain densities are similar to those of the reference mixtures (Table 10), indicating similarity in closed porosity for these samples.

The observation of elongated grains in the palygorskite paste indicates that the C–S–H has probably formed on the palygorskite particle surfaces. For the palygorskite pastes, the grain densities (Table 10) are fairly close to those of the reference pastes indicating similarity in closed porosity.

The total amount of C–S–H is the same in all samples, as judged from the equal amounts of non-evaporable water released at 180 °C (Table 6). The palygorskite and bentonite pastes contain larger amounts of physically adsorbed water assigned to interlayers in C–S–H (Table 4) as compared to the silica fume, kaolinite, and reference pastes. This indicates a more open structure of the C–S–H in the palygorskite and bentonite pastes, a conclusion which is supported by the larger specific surface areas (Table 2) and the larger helium porosities (Table 6) for these pastes. Similarly, the amount of capillary water is larger for the palygorskite and bentonite pastes (Table 4), demonstrating a more open paste structure for these mixtures. These differences can be attributed to the growth of C–S–H on the micro- and nano-sized clay particles. This strongly suggests that the particle size of the added clay to a large extent determines the porosity characteristics of the pastes, not only by the particle size as such, but also as a result of the growth of C–S–H on the particle surfaces. A consequence of the modified nanostructure for the palygorskite and bentonite pastes is that physically adsorbed and evaporable water will have escape outlets in these pastes during heating.

The new type of cementitious material obtained by adding the clay micro- and nano-fillers may be employed in concrete structures where transport by diffusion in an open nano-pore system is preferred compared to a material having large pores of which a substantial proportion is closed, such as in materials with silica fume addition.

## 4. Conclusions

The present work has shown that it is possible to engineer cement paste structures by addition of clay materials without pozzo-

lanic properties. The results are accomplished by investigations of pastes and mortars of a white Portland cement and of this cement including additives of silica fume, kaolinite, bentonite, and palygorskite using a number of different techniques. Furthermore, the degree and duration of sample drying have been found to strongly modify the structure of the cementitious material under investigation. Pastes having been rapidly dried, e.g., under high vacuum at room temperature, are likely to be closest in structure to the untreated cement pastes. The specific surface area and the volume of fine (diameter <200 Å) pores have been determined by nitrogen adsorption and the total porosity by helium porosimetry. The largest values of surface area and porosity are obtained for pastes and mortars that include palygorskite or bentonite as additive. DTA-evolved water analysis of pastes has shown that the amounts of non-evaporable, total evaporable and physically adsorbed water are largest in the pastes including bentonite and palygorskite. This is supported by low-temperature calorimetry, which indicates that the amounts of evaporable water and of water in capillary and intraglobular pores are largest for mortars with the palygorskite and bentonite additives. Atomic force microscopy (AFM) of raw paste surfaces at room conditions imaged globular grains and irregularly shaped pores. Clay particles could not be observed in the hydrated materials, probably because the cement hydration products have crystallised on the surface of the clay minerals. In addition, layered structures were observed in the AFM images of the hydrated samples and tentatively assigned to C–S–H. This suggests that the C–S–H growth on the clay particle surfaces results in structures determined by the size and shape of the clay particles and the negative charge of some of the clay minerals and thereby that it is possible to engineer cement paste structures and porosities by addition of non-pozzolanic clays. The effects of clay addition on Portland cement hydration are more pronounced for palygorskite and bentonite than for kaolinite. This reflects that bentonite and palygorskite have the largest surface areas and negative charges on the particle surfaces. Compared to the reference and kaolinite pastes, the palygorskite and bentonite pastes have a more open pore structure consisting of interconnected fine pores. Silica fume paste contains a significant proportion of closed pores. In mortars with clays added the interfacial transition zone (ITZ) is connected to the system of interconnected fine pores.

## Acknowledgements

The Danish Technical Research Council (STVF) is acknowledged for their support through the project: "New concretes through addition of layer silicates" (No. 2020-00-0005). We thank Director A. Henrichsen, Dansk Beton Teknik A/S, for fruitful discussions.

## References

[1] Diamond S. Aspects of concrete porosity revisited. Cem Concr Res 1999;29:1181–8.
[2] Richardson IG. Tobermorite/jennite and tobermorite/calcium hydroxide-based models for the structure of C–S–H: applicability to hardened pastes of tricalcium silicate, β-dicalcium silicate, Portland cement, and blends of Portland cement with blast-furnace slag, metakaolin, or silica fume. Cem Concr Res 2004;34:1733–77.
[3] Juenger MCG, Jennings HM. The use of nitrogen adsorption to assess the microstructure of cement paste. Cem Concr Res 2001;31:883–92.
[4] Taylor HFW. Cement chemistry. 2nd ed. London, UK: Thomas Telford Publishing; 1997.
[5] Cong X, Kirkpatrick RJ. $^{17}O$ MAS NMR investigation of the structure of calcium silicate hydrate gel. J Am Ceram Soc 1996;79:1585–92.
[6] Feldman RF, Sereda P. A new model for hydrated Portland cement and its practical applications. Eng J Can 1970;53:53–69.
[7] Jennings HM. A model for the microstructure of calcium silicate hydrate in cement paste. Cem Concr Res 2000;30:101–16.
[8] Tennis PD, Jennings HM. A model for two types of calcium silicate hydrate in the microstructure of Portland cement pastes. Cem Concr Res 2000;30:855–63.
[9] Jennings HM, Thomas JJ. A discussion of the paper "The BET-specific surface area of hydrated Portland cement and related materials" by Ivan Odler. Cem Concr Res 2004;34:1960–1.
[10] Scrivener KL. Backscattered electron imaging of cementitious microstructures: understanding and quantification. Cem Concr Compos 2004;26:935–45.
[11] Bentz DP, Jensen OM, Coats AM, Glasser FP. Influence of silica fume on diffusivity in cement-based materials. I. Experimental and computer modeling studies on cement pastes. Cem Concr Res 2000;30:953–62.
[12] Bentz DP. Fibers, percolation and spalling of high-performance concrete. ACI Mater J 2000;97:351–9.
[13] Kalifa P, Menneteau FD, Quenard D. Spalling and pore pressure in HPC at high temperatures. Cem Concr Res 2000;30:1915–27.
[14] Hertz KD. Limits of spalling of fire-exposed concrete. Fire Safety J 2003;38:103–16.
[15] Krøyer H, Lindgreen H, Jakobsen HJ, Skibsted J. Hydration of Portland cement in the presence of clay minerals studied by $^{29}Si$ and $^{27}Al$ MAS NMR spectroscopy. Adv Cem Res 2003;15:103–12.
[16] Beedle SS, Groves GW, Rodger SA. The effect of fine pozzolanic and other particles on the hydration of $C_3S$. Adv Cem Res 1989;2:3–8.
[17] Manic V, Miljkovic I, Djuric-Stanojevic B. The $^1H$ $T_1$ study of the influence of clay addition on Portland cement hydration. Appl Magn Res 1997;13: 231–9.
[18] Moukwa M, Lewis BG, Shah SP, Ouyang C. Effects of clays on fracture properties of cement-based materials. Cem Concr Res 1993;23:711–23.
[19] He C, Osbæck B, Mackovicky E. Pozzolanic reactions of six principal clay minerals: activation, reactivity, assessments and technological effects. Cem Concr Res 1995;25:1691–702.
[20] He C, Osbæck B, Mackovicky E. Thermal stability and pozzolanic activity of raw and calcined mixed-layer mica/smectite. Appl Clay Sci 2000;17:141–61.
[21] Morgan DJ. Simultaneous DTA-EGA of minerals and natural mineral admixtures. J Thermal Anal 1977;12:245–63.
[22] Dweck J, Buchler PM, Coelho ACV, Cartledge FK. Hydration of Portland cement blended with calcium carbonate. Thermochim Acta 2000;346:105–13.
[23] Hagymassy J, Odler I, Yudenfreund M, Skalny J, Brunauer S. Pore structure analysis by water vapor adsorption. III. Analysis of hydrated calcium silicates and Portland cements. J Colloid Interface Sci 1972;38:20–34.
[24] Gregg SJ, Sing KSW. Adsorption surface area and porosity. London: Academic Press; 1967.
[25] API RP 40. Recommended practice for core analysis. 2nd ed. American Petroleum Institute; 1998.
[26] NT Build 492. Concrete, mortar and cement-based repair materials: chloride migration coefficient from non-steady-state migration experiments. NordTest, approved 1999-11.
[27] Fontenay le Sage de C, Sellevold EJ. Ice formation in hardened cement pastes – I. Mature water-saturated pastes. Durability of building materials and components. ASTM STP 691; 1980.
[28] Bager D, Sellevold EJ. Ice formation in hardened cement paste, Part I – Room temperature cured pastes. Cem Concr Res 1986;16:709–20.
[29] Sellevold EJ, Bager D. Low temperature calorimetry as a pore structure probe. In: 7th international congress on the chemistry of cement, Paris, vol. 4; 1981.
[30] Feldman RF. Pore structure damage in blended cements caused by mercury intrusion. J Am Ceram Soc 1984;67:30–3.
[31] Diamond S. Review: mercury porosimetry. An inappropriate method for the measurement of pore size distributions in cement-based materials. Cem Concr Res 2000;30:1517–25.
[32] Lion M, Skoczylas F, Lafhaj Z, Sersar M. Experimental study on a mortar. Temperature effects on porosity and permeability. Residual properties or direct measurements under temperature. Cem Concr Res 2005;35:1937–42.
[33] Gran HC, Hansen EW. Effects of drying and freeze/thaw cycling probed by $^1H$ NMR. Cem Concr Res 1997;27:1319–21.
[34] Odler I. The BET-specific surface area of hydrated Portland cement and related materials. Cem Concr Res 2003;33:2049–56.
[35] Rarick RL, Thomas JJ, Christensen BJ, Jennings HM. Deterioration of the nitrogen BET surface area of dried cement paste with storage time. Adv Cem Based Mater 1996;3:72–5.
[36] Galle C. Effect of drying on cement-based materials pore structure as identified by mercury intrusion porosimetry. A comparative study between oven-, vacuum-, and freeze-drying. Cem Concr Res 2001;31:1467–77.
[37] Abell AB, Willis KL, Lange DA. Mercury intrusion porosimetry and image analysis of cement-based materials. J Colloid Interface Sci 1999;211:39–44.
[38] Stepkowska ET, Blanes JM, Real C, Perez-Rodriguez JL. Hydration products in two ages cement pastes. J Thermal Anal Cal 2005;82:731–9.
[39] Mackenzie RC. Simple phyllosilicates based on gibbsite- and brucite-like sheets. In: Mackenzie RC, editor. Differential thermal analysis, vol. 1. Academic Press; 1970. p. 498–538.
[40] Feldman RF, Ramachandran VS. Differentiation of interlayer and adsorbed water in hydrated Portland cement by thermal analysis. Cem Concr Res 1971;1:607–20.
[41] Feldman RF. Application of the helium inflow technique for measuring surface area and hydraulic radius of hydrated Portland cement. Cem Concr Res 1980;10:657–64.
[42] Bentz DP. A three-dimensional cement hydration and microstructure program. I. Hydration rate, heat of hydration, and chemical shrinkage. National Institute of Standards and Technology, NISTIR 5756; 1995.
[43] Groves GW, Richardson IG. Microcrystalline calcium hydroxide in pozzolanic cement pastes. Cem Concr Res 1994;24:1191–6.

[44] Richardson IG. The nature of the hydration products in hardened cement pastes. Cem Concr Compos 2000;22:97–113.
[45] Bodor EE, Skalny J, Brunauer S, Hagymassy J, Yudenfreund M. Pore structures of hydrated calcium silicates and Portland cements by nitrogen adsorption. J Colloid Interface Sci 1970;34:560–70.
[46] Winslow DN, Bukowski JM, Young JF. The early evolution of the surface of hydrating cement. Cem Concr Res 1994;24:1025–32.
[47] Odler I, Chen Y. Investigations on the ageing of hydrated tricalcium silicate and Portland cement pastes. Cem Concr Res 1995;25:919–23.
[48] Bager D, Sellevold EJ. Ice formation in hardened cement paste, Part II – Drying and resaturation on room temperature cured pastes. Cem Concr Res 1986;16:835–44.
[49] Kjeldsen AM, Geiker MR. On the interpretation of low temperature calorimetry data. Mater Struct 2008;41:213–24.
[50] Bager D. Ice formation in hardened cement paste. Technical report 141/84. Technical University of Denmark; 1984.
[51] Snyder KA, Bentz DP. Suspended hydration and loss of freezable water in cement pastes exposed to 90% relative humidity. Cem Concr Res 2004;34:2045–56.
[52] Bentz DP, Stutzman PE. Evolution of porosity and calcium hydroxide in laboratory concretes containing silica fume. Cem Concr Res 1994;24:1044–50.